Diapycnal Upwelling Driven by Tidally Induced Mixing over Steep Topography

XIAOZHOU RUAN,[a] YIDONGFANG SI,[b] AND RAFFAELE FERRARI[b]

[a] *Department of Earth and Environment, Boston University, Boston, Massachusetts*
[b] *Department of Earth, Atmospheric, and Planetary Sciences, Massachusetts Institute of Technology, Cambridge, Massachusetts*

(Manuscript received 13 January 2024, in final form 18 November 2024, accepted 31 December 2024)

ABSTRACT: Diapycnal upwelling along sloping topography has been shown to be an important component of the abyssal overturning circulation. Theoretical studies of mixing-driven upwelling have mostly relied on a time-averaged description of mixing acting on a mean stratification which ignores the intermittency of mixing. Typically, these studies prescribed a time-invariant turbulent diffusivity profile motivated by scenarios where tidal currents encounter gentle topography with small-scale corrugations, leading to subsequent propagation and breaking of internal waves. Here, a different scenario is considered where a tidal current interacts with smooth but steep topography, a case often encountered near continental margins and troughs. The performed nonhydrostatic simulations resolve both the strong oscillatory shear that develops along the steep critical topography and the associated mixing events. Strong diapycnal mixing is observed during the upslope phase of the tidal flow when both the near-boundary stratification and shear are enhanced. During the downslope phase, strong overturning events do develop, but they are associated with weak stratification and less efficient diapycnal mixing. These results highlight that the temporal evolution of both shear and stratification play a key role in setting when diapycnal mixing and water mass transformation occur along steep topography. In contrast, over gentle topography, tidal shears do not become sufficiently large to generate strong local mixing for typical oceanographic parameters.

KEYWORDS: Diapycnal mixing; Turbulence; Boundary layer; Tides

1. Introduction

Dense waters, formed through buoyancy loss at high latitudes, continuously sink to the ocean bottom, transporting vast amounts of carbon and heat along their pathway (Lumpkin and Speer 2007; Talley 2013). In steady state, these waters must move across density layers to return to the surface as less dense waters (Munk 1966; Ferrari 2014). The rate at which waters cross density surfaces, and the associated transport of carbon and heat, is proportional to the intensity of turbulent mixing between light and dense waters, which is quantified by turbulent diffusivity. While the importance of turbulent mixing in shaping the abyssal ocean circulation has been recognized since the early days of modern oceanography (Stommel 1957; Munk 1966), direct evidence of vigorous mixing in the abyssal ocean has only become available in the last couple of decades (Polzin et al. 1997; Ledwell et al. 2000; Waterhouse et al. 2014). These observations paint a picture of strong mixing events that are very intermittent and primarily confined above rough sloping topography where subinertial and tidal currents interact with the seafloor. Recent observations and numerical studies suggest that these mixing events are driven by various processes, including the breaking of internal tides associated with convective or shear instabilities (e.g., Legg and Adcroft 2003; Legg and Huijts 2006; Legg and Klymak 2008; Klymak et al. 2010; Klymak and Legg 2010; Jalali et al. 2017; van Haren et al. 2022, 2024), nonlinear wave–wave interactions (e.g., Nikurashin and Legg 2011), as well as the propagation of internal tidal bores (e.g., Winters 2015; Dauhajre et al. 2021; van Haren 2023a). However, a comprehensive understanding of the intricate mixing patterns near sloping seafloors, driven by local velocity shear from barotropic tide reflection, is still lacking, particularly regarding mixing efficiency and near-bottom water mass transformation.

The Brazil Basin Tracer Release Experiment (BBTRE) provided the first direct evidence of the strong water mass conversions along sloping topography (St. Laurent et al. 2001; Polzin 2009). Microstructure profiles of temperature and shear variance documented that turbulent mixing associated with breaking internal waves was strongly enhanced within a few hundred meters of the rough seafloor of the Mid-Atlantic Ridge (MAR) and was associated with the interaction of the barotropic tidal flows with the corrugated topography over the flank of the MAR. Turbulent mixing was much weaker over the smooth abyssal plains and continental margins of the Brazil Basin (Polzin et al. 1997). A concurrent tracer release experiment confirmed that the turbulent mixing resulted in flows and transport across isopycnals (Ledwell et al. 2000). The observations depicted a scenario where the internal waves radiating from a corrugated and mildly sloping topography interacted nonlinearly and generated intermittent wave–breaking events randomly distributed above the topography. Averaged over many tidal periods, this resulted in a continuous profile of mixing decaying with height above the bottom (HAB). The mixing profile increasing in intensity toward the rough MAR seafloor further implied a dipole pattern of diapycnal downwelling in response to the divergent buoyancy flux above topography and diapycnal upwelling along the seafloor where the buoyancy flux became convergent to satisfy the no-normal-flux boundary condition (St. Laurent et al. 2001; Polzin 2009). This pattern proved consistent with the idealized solutions of diapycnal flows driven by mixing above smooth sloping boundaries studied by Garrett et al. (1993). More recently, Ferrari et al. (2016) and de Lavergne et al. (2016) argued that the upwelling/downwelling dipole is

Corresponding author: Xiaozhou Ruan, xruan@bu.edu

DOI: 10.1175/JPO-D-24-0008.1

ubiquitous above rough topography and determines the very structure and magnitude of the global meridional overturning circulation (Callies and Ferrari 2018).

Elevated mixing associated with the breaking of internal tides has been observed near topographic features, such as steep ridges (e.g., Klymak et al. 2006; Alford et al. 2011) and rough continental slopes (e.g., Moum et al. 2002; Nash et al. 2007; Martini et al. 2013). Here, a different scenario of turbulent mixing above topography is studied, one in which the barotropic tide encounters smooth topography whose slope is close to, or larger than, the natural internal wave propagation angle, the so-called critical slope. Such topographic slopes are often encountered along continental margins and troughs, which can be very steep but smoother than the geologically younger and rougher ridges and seamounts. Nash et al. (2007) observed some exceptionally large dissipation rates over smooth topography over the Oregon slope with minimal local bottom roughness and suggested that these could result from interactions between internal tides and near-critical bathymetry. Turbulence along smooth, but steeply sloping topography, has also been the focus of the recent Rockall Trough bottom boundary layer turbulence (BLT) experiment. Preliminary results suggest that the observed mixing and water mass transformation patterns are very different from those reported in BBTRE (Wynne-Cattanach et al. 2024). When the barotropic tide impinges on a smooth critical slope, instead of being converted into a field of shorter internal waves, it drives a strong current along the seafloor that reverses directions at the tidal frequency (Dauxois and Young 1999). This bottom-trapped current is strong enough to generate a periodic sequence of convective and shear instabilities in different phases of the tidal cycle right above the topography. The rest of this study focuses on this scenario.

The time-dependent mixing scenario is studied with an idealized numerical model. A barotropic tidal flow is imposed through a reversing body force in the momentum equation. The topography has a smooth sinusoidal shape. The tidal flow generates strong shears above the seafloor which differentially advect isopycnals back and forth across topographic slopes, periodically enhancing and reducing the stratification of the boundary layer. For steep slopes, the shear becomes sufficiently strong during the upslope phase of the tide to drive the Richardson number below approximately a quarter (Howard 1961; Miles 1961) and leads to a burst of diapycnal mixing. During the downslope phase, the differential advection brings light water under dense water, reduces the stratification resulting in large convective overturns but little diapycnal mixing. The net result is a transformation of waters from dense to light, but through a well-timed sequence of mixing bursts rather than a continuous process. The addition of time dependence is the key difference in this study compared to the steady solutions described by Garrett (1979).

The manuscript is organized as follows. We introduce the nonhydrostatic numerical model of a barotropic flow impinging on a sloping topography in section 2 and discuss the resulting dynamics which include turbulent mixing and the associated water mass transformation in section 3. The diapycnal upslope flow is further illustrated by releasing numerical tracers just above the seafloor in section 4. Finally, we discuss the implications of our work for the abyssal water mass transformation in section 5.

2. Numerical model setup

We set up nonhydrostatic simulations with the Massachusetts Institute of Technology General Circulation Model (MITgcm; Marshall et al. 1997). The physics we aim to investigate include reflection of tidal flows at a sloping topography, tidal modulation of local stratification, and shear-driven mixing and convection. Since two-dimensional (2D) models have been widely used in previous studies to qualitatively capture these processes (e.g., Legg and Adcroft 2003; Legg and Klymak 2008; Klymak et al. 2010; Buijsman et al. 2012) and three-dimensional (3D) nonhydrostatic simulations are computationally expensive, our analysis will primarily focus on 2D. A tidal force is applied by introducing a body force term into the momentum equations, which, in the inviscid limit, leads to an oscillatory barotropic flow,

$$u(t) = U_0 \sin\omega t, \tag{1}$$

$$v(t) = \frac{fU_0}{\omega} \cos\omega t, \tag{2}$$

where f and ω are the Coriolis and tidal frequencies and U_0 is the tidal amplitude. The Coriolis frequency is set to $f = 0.53 \times 10^{-4}$ s^{-1}, corresponding to a latitude of approximately 21°. Typical tidal velocities in the ocean abyss are of a few centimeters per second. We set $U_0 = 2.5 \times 10^{-2}$ m s^{-1} (Polzin 2009) as representative of a moderate tidal flow. The frequency of the barotropic forcing is set to the semidiurnal tidal frequency M2, the dominant tidal constituent at low- and midlatitudes, $\omega = 1.454 \times 10^{-4}$ s^{-1}. These values are representative of the Brazil Basin, but the simulations are not designed to represent a specific region but rather to explore different dynamical regimes. For example, we will consider topographic slopes much steeper than those encountered in the Brazil Basin.

The seafloor depth h varies according to the sinusoidal function:

$$h(x) = H + A \cos(2\pi x/L_x), \tag{3}$$

where $H = -1945$ m, $L_x = 15$ km is the horizontal extent of the model domain, and A sets the amplitude of the sinusoidal topography—see Fig. 1. We consider two values of A, 400 and 200 m, as examples of steep and gentle slopes (Fig. 1). The domain is horizontally periodic with a uniform horizontal grid spacing of $\Delta x = 20$ m. The vertical grid spacing is uniform in the bottom 1600 m with $\Delta z = 3$ m, while Δz progressively increases in the upper 750 m where a sponge layer is imposed to absorb upward-radiating internal waves. Partial cells are implemented at topography with cell thickness as small as 0.9 m.

Buoyancy is set to be a linear function of temperature, and the simulations are initialized with a constant vertical stratification of $N^2 = 10^{-6}$ s^{-2}. The slope of the internal wave characteristic is given by

$$\tan\theta_c = \left(\frac{\omega^2 - f^2}{N^2 - \omega^2}\right)^{1/2}, \tag{4}$$

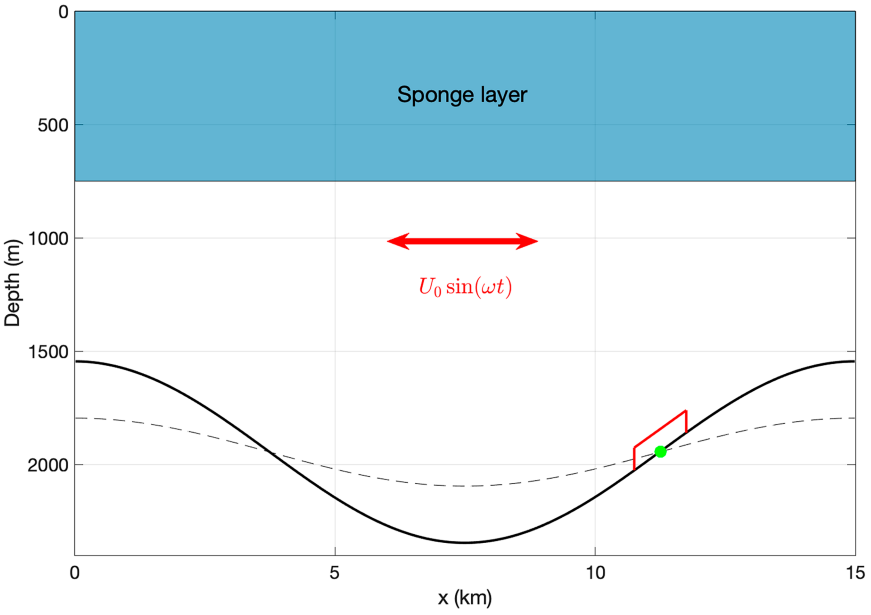

FIG. 1. Schematic of the numerical model setup. A barotropic tidal forcing of amplitude U_0 and frequency ω is applied everywhere in the model domain. The black solid and dashed curves represent the two sets of sinusoidal topographies used in the study with amplitudes $A = 400$ and $A = 200$ m. The location with the maximum slope is marked by the green dot. The time series in Fig. 2 are computed at this location. The red lines mark the boundary of the control volume used in the following volume average budgets.

and it is equal to 0.137 using the initial stratification. The maximum topographic slope at the midslope location for the runs with $A = 400$ m is $\theta = 0.168$ (Fig. 1), making the topographic slope supercritical to internal wave reflections over a limited depth range. For $A = 200$ m, the slope is everywhere subcritical. We run nonhydrostatic simulations in order to (partially) resolve the tidal mixing induced by hydrodynamic instabilities. Constant background viscosity and diffusivity are applied, $\nu_v = \kappa_v = 2 \times 10^{-4}$ m^2 s^{-1} and $\nu_h = \kappa_h = 1 \times 10^{-4}$ m^2 s^{-1}, where the subscripts ν and h denote the vertical and horizontal directions; no additional subgrid-scale closure is employed. These background values are at least one order of magnitude smaller than the diagnosed turbulent viscosity/diffusivity in the simulations. The time step is $\Delta t = 5$ s throughout all runs. No-flux boundary conditions are applied for buoyancy and other tracers at the seafloor. The free-slip condition together with a quadratic bottom drag is used for momentum at the seafloor with a drag coefficient of $C_d = 2.5 \times 10^{-3}$.[1] All analyses are based on simulation results after an initial spinup period of 25 days to avoid the initial adjustment of the near-boundary stratification which starts with flat density surfaces that rapidly bend toward the topography to satisfy the no-flux boundary condition. The mean stratification thus weakens after the initial adjustment, and the slope of reflected internal waves becomes near critical for the $A = 400$ m simulation.

3. Tidal flows, mixing, and water mass transformation

a. *Basic flow fields and turbulent mixing*

We start by discussing the evolution of the simulated flow and stratification because they provide the context to interpret the turbulent mixing and water mass transformation along the sloping boundary. The temporal evolution of the horizontal flow u and the stratification N^2 as a function of height above the bottom at the midslope ($x = 11.25$ km) is shown for both the subcritical and supercritical slope simulations in Fig. 2. In the subcritical slope simulation, a weak shear develops within 15 m of the bottom, where the bottom drag slows down the tidal flow. This shear is hardly visible in the velocity plot (Fig. 2a), but its effect is clear in the evolution of stratification through differential advection (Fig. 2b). Within this thin 15-m layer, N^2 increases when the tidal flow is downslope (negative) and the shear is negative, and thus acts to restratify the bottom waters, while N^2 decreases when the tidal flow is upslope (positive) and the positive shear reduces the bottom stratification. Following coastal dynamics terminology, we will refer to the upslope/downslope tidal phases as the "flood"/"ebb" phases. The velocity and stratification signals are equal and opposite in the flood and ebb phases, suggesting that the dynamics is approximately linear and follows the periodicity of the forcing. The slight delay (a quarter

[1] Combining no-slip conditions with quadratic drag in MITgcm results in nonphysical double counting of bottom friction, exceeding the effect of quadratic drag alone. Additionally, simulation results show minimal sensitivity to the specific combination used, as the highest velocities consistently occur some distance above the seafloor.

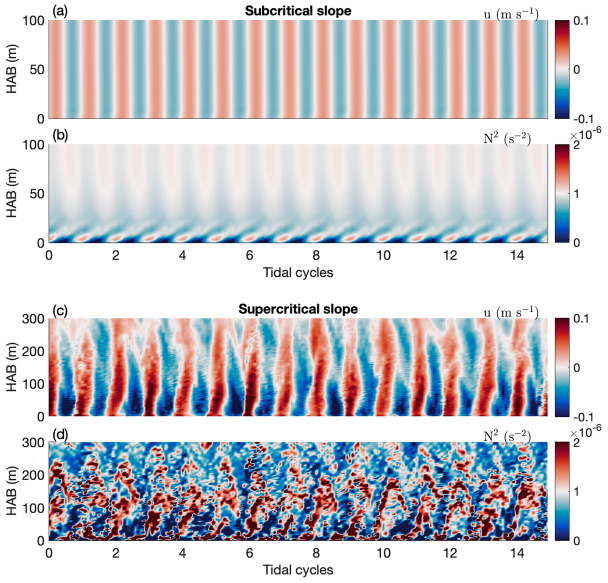

FIG. 2. Time series of (a),(c) zonal velocity u and (b),(d) stratification N^2 as a function of HAB at the midslope location (green dot in Fig. 1) over (top) subcritical and (bottom) supercritical slopes.

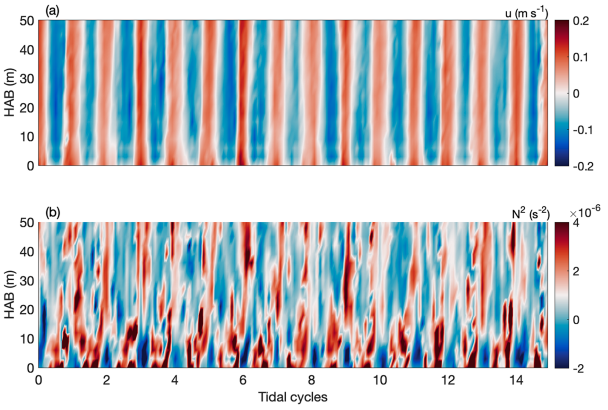

FIG. 3. Time series of (a) zonal velocity u and (b) stratification N^2 as a function of HAB at the midslope location (green dot in Fig. 1) over supercritical slopes. Note that the color scales are different from those in Fig. 2.

period to be exact) between the onset of positive/negative shear and weak/strong stratification reflects the fact that it is the rate of change of stratification $\partial_t N^2$, rather than stratification N^2 itself, that responds to the tidal shear and the two are offset by a quarter period.

In the supercritical slope simulation, the reflection of the barotropic tide along the boundary results in a strong bottom-intensified velocity over a 200-m thick layer reversing direction at the tidal frequency—see Fig. 2c—consistent with internal wave reflection at near-critical slopes (Eriksen 1982; Dauxois and Young 1999; Pedlosky 2003). Within ~15 m of the seafloor, bottom drag slows down the velocity like in the subcritical case. This results in a velocity profile whose magnitude increases up to a maximum at ~15 m above the seafloor and then decreases with height above the bottom—see Figs. 2c and 3a and the schematic in Fig. 4. As a result, the stratification evolution shows opposite trends within ~15 m of the seafloor and the thick layer above (Fig. 3). In the thin layer near the seafloor, stratification decreases during the flood phase due to the positive velocity shear, while just above it, stratification grows due to the negative velocity shear (Figs. 2c,d, 3, and 4). Strong mixing patches develop near the seafloor that propagate up the slope in what has been described as a bore in both numerical simulations and observations of tidal flows over steep topography (e.g., Slinn and Riley 1996; Legg and Adcroft 2003; van Haren 2006; Winters 2015). During the ebb phase, stratification increases within the thin ~15-m layer, but above the tidal shear brings a plume of light water down the slope and reduces the stratification. This results in convective plumes of light waters rising up to 150 m aloft which reduce both stratification and shear, thereby shifting upward the velocity maximum as seen in Fig. 2c, blue color. The flow field in the simulations is smoother compared to that reported in observations (e.g., van Haren 2023b), which is likely a result of the smooth topography used in the model. Additional simulations above constant supercritical slopes reveal similar phase coupling between velocity (shear) and stratification throughout the tidal cycle. Notably, toward the end of the sinusoidal

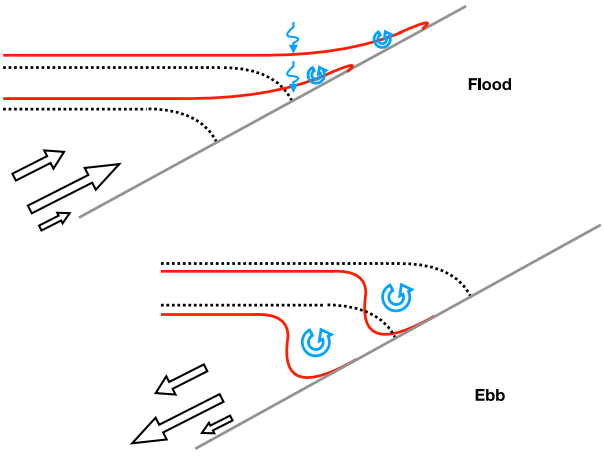

FIG. 4. Schematic of isopycnal profiles during two phases of a tidal cycle over steep topography. The black dotted and red solid curves represent isopycnals at the initial and end states of each phase of the tidal cycle. The arrows denote the direction and magnitude of the cross-slope velocities. During the flood phase, dense water is advected upslope which results in a stronger stratification which is overcome by the bottom shear and results in shear-driven mixing and a strong buoyancy flux (blue squiggly arrows) that extends from the seafloor to somewhat above the drag-controlled thin layer. During the ebb phase, local stratification becomes weak as dense waters are advected downslope under light water. Although the local turbulence intensity and energy dissipation rate are enhanced due to gravitational instability, the buoyancy flux is weak because the mixing is acting on weakly stratified waters. The very thin layers close to the bottom have different stratification from those in the much thicker layers above due to the presence of bottom drag.

slope, as it flattens, we observe a shift in velocity shear from negative to positive above the bottom thin layer during the flood phase and from positive to negative in the ebb phase. This shift occurs as the critical reflected tidal beam, initially parallel to the steepest part of the topography, lifts off the bottom, and extends into the water column where the slope becomes more gradual. The influence of bottom topography curvature will be explored in a future study.

We quantify the mixing by diagnosing the dissipation rate of turbulent kinetic energy (TKE), defined as $\epsilon = \nu_i(\partial u_j/\partial x_i)^2$ and the dissipation rate of temperature variance $\chi_T = \kappa_i|\partial x_i T|^2$, where T is the potential temperature and i and j are the summation indices. These are common mixing diagnostics with the former representing the intensity of turbulent motions and the latter denoting the rate at which these motions drive irreversible mixing across isotherms. We estimate ϵ and χ_T over a control volume centered over the midslope extending 1 km in the horizontal and 100 m in the vertical (the red box in Fig. 1), a volume that encompasses the steepest slope region. The volume average will be indicated as angle brackets, $\langle\epsilon\rangle$ and $\langle\chi_T\rangle$. We discuss only results for the supercritical case because little turbulence is generated in the subcritical case. This is true even for larger tidal amplitudes (we considered tidal flows up to 0.2 m s^{-1}). The mixing diagnostics are computed using pointwise model output in the calculation of the various gradients and do not include numerical mixing. We have also compared this explicitly calculated mixing rate with the total mixing rate, which encompasses both the resolved component and numerical mixing (details in appendix A). The results indicate that explicit mixing dominates the total mixing rate, suggesting that our resolutions can capture the dominant small-scale physics.

In the supercritical case, $\langle\epsilon\rangle$ peaks during the ebb phase, more specifically at the end of the ebb phase (Fig. 5a), while $\langle\chi_T\rangle$ peaks during the flood phase when the shear is largest (Fig. 5b). In the ocean interior, where mixing is primarily driven by breaking internal waves, the mixing coefficient Γ is often approximated as a constant to represent the averaged value throughout a mixing cycle (e.g., Gregg et al. 2018). This ratio represents the fraction of TKE that is expended into raising potential energy during a mixing event. Here, we calculate the bulk mixing coefficient Γ_{bk} using instantaneous volume-averaged dissipation rates of temperature variance and TKE (Smyth et al. 2001):

$$\Gamma_{bk} = \frac{\alpha g}{2\langle\partial_z T\rangle}\frac{\langle\chi_T\rangle}{\langle\epsilon\rangle}, \tag{5}$$

where $\alpha = 2\times10^{-4}\,^{\circ}\mathrm{C}^{-1}$ is the thermal expansion coefficient, Γ_{bk} becomes as large as 0.15 during the flood phase, while it drops to approximately 0.05 or below during the ebb phase (Fig. 5c). The larger mixing coefficient is slightly below the canonical value of 0.2, partly due to the volume-averaging process that smooths out peak values, and the relatively coarse resolution may miss the finest-scale velocity shear and density fluctuations, which are critical for this calculation. The key point is that there is a transition between high and low values of mixing coefficients between the two phases of the tidal

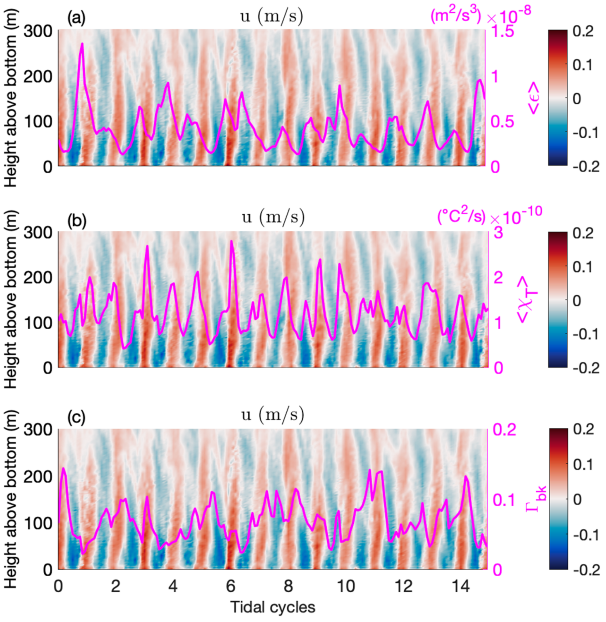

FIG. 5. Time series of (a) volume-averaged TKE dissipation rate $\langle\epsilon\rangle$, (b) destruction rate of temperature variance $\langle\chi_T\rangle$, and (c) bulk mixing coefficient Γ_{bk} on top of the zonal velocity over the midslope location.

cycle. The exact values should be taken with caution because they are computed from 2D simulations. Direct numerical simulation (DNS)/LES simulations with sufficient resolution to capture full 3D turbulence would be needed to investigate the quantitative differences. Nonetheless, the qualitative difference is to be expected given the differences in the sources of turbulence between the two phases. The larger mixing coefficient in the flood phase highlights the importance of the time dependence of tidally modulated shear-driven mixing, which sets the stage for the recurrent formation of young overturns in each tidal cycle, characterized by a large Γ_{bk} (Peltier and Caulfield 2003; Mashayek et al. 2017). A smaller ratio during the ebb phase is not a surprise because the energy pathway is distinct from that of the shear instabilities that develop during the flood phase. During the ebb phase, the energy that drives the convective overturns is supplied by the differential advection of light fluid under dense by the tidal shear (Fig. 4). The resulting convective overturns generate both TKE (the plumes) and potential energy (mixing). However, the amount of potential energy generated is small because convection develops when the mean stratification has been reduced to nearly zero by the tidal shear. We note that a similar analysis conducted in a 3D domain yielded qualitatively consistent results, showing that Γ_{bk} is higher during the flood phase than during the ebb phase.[2]

[2] The simulation domain is extended in the along-slope direction for a total of 300 m with the same horizontal resolution as in the cross-slope direction and is initialized with the temperature field from the 2D simulation on day 25 after the isotherms had adjusted to bend to satisfy the no-normal flux boundary condition at the seafloor.

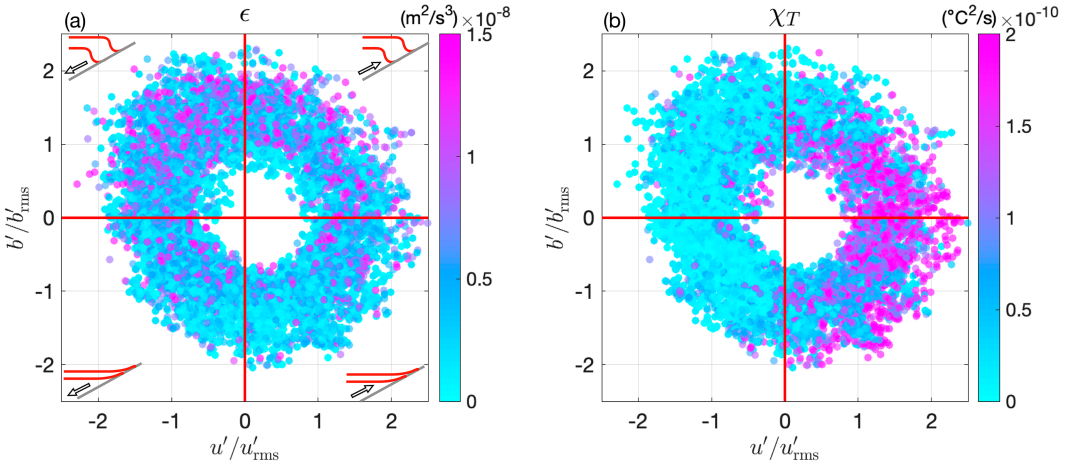

FIG. 6. The distribution of u' and b' from instantaneous (hourly) output in the supercritical slope case with representative samples colored by their (a) ϵ and (b) χ_T values. The samples are taken between $x = 10.75$ km and $x = 11.75$ km (centered around the midslope location) and 30 m above the bottom. The red curves and black arrow in the schematic of each quadrant in (a) represent isopycnals and the direction of cross-shore velocity.

A complete tidal cycle is segmented into four quadrants, determined by the relationship between velocity and buoyancy anomalies in comparison with their time-averaged values. We plot pointwise values of these anomalies at a fixed elevation of 30 m above the seafloor within the control volume and color them by their ϵ and χ_T values in the two panels of Fig. 6. This offers a detailed depiction of the sequencing of the two mixing diagnostics. Specifically, ϵ is strong in the upper two quadrants when isopycnals are tilted downward, and it reaches its maximum in the second quadrant, as the negative velocity during the ebb phase pushes isopycnals downslope and triggers convection (Fig. 6a). In contrast, χ_T reaches its peak value when the positive velocity reaches its maximum and specifically when the buoyancy anomaly becomes negative due to the isopycnals being advected upslope beyond their time-mean position from the first to the fourth quadrant (Fig. 6b). This presentation of the data confirms that stronger bursts of turbulence occur toward the end of the ebb phase, while more efficient mixing takes place during the flood phase when the strong velocity shear and background stratification couple.

An important implication of our analysis is that the two traditional measurements of turbulent motions, ϵ and χ_T, can actually peak in different phases of the tidal cycle in regions of tidally driven mixing along the seafloor. In oceanographic literature, an average value of $\Gamma = 0.2$ is often suggested as a reasonable representation of a complete mixing event (e.g., Peltier and Caulfield 2003; Gregg et al. 2018). However, our simulations show that this averaged mixing coefficient does not accurately represent mixing throughout the tidal cycle, with the ebb phase exhibiting notably less efficient mixing. Thus, for this study, it makes little sense to define an average mixing coefficient for the entire tidal cycle because it comprises two distinct mixing processes. These substantial differences in the mixing coefficient during different tidal phases highlight the need for high-frequency measurements to capture the variations in mixing statistics.

b. *Water mass transformation*

In addition to identifying mixing patterns across various tidal phases, we are interested in estimating the resulting water mass transformation. For robustness, we assess the diapycnal transport over a 5-day period, employing methods that include the calculation of horizontal mass transport and tracking changes in isopycnal positions. Following Schmidgall et al. (2023), we start by computing the horizontal transport below the potential temperature surface $\mathbb{T}$,

$$U(x, \mathbb{T}, t) = \int_{z=-h}^{z=0} u(x, z, t)\mathcal{H}[\mathbb{T} - T(x, z, t)]dz, \tag{6}$$

where $z = -h$ is the bottom topography, $z = 0$ is the ocean surface, u is the model horizontal velocity, $\mathcal{H}[\cdot]$ is the Heaviside step function, and $T(x, z, t)$ is the simulated potential temperature. Next, we compute the height of the instantaneous isopycnal above the bottom,

$$h_{\text{iso}}(x, \mathbb{T}, t) = \int_{z=-h}^{z=0} \mathcal{H}[\mathbb{T} - T(x, z, t)]dz. \tag{7}$$

The diapycnal velocity across the potential temperature surface $\mathbb{T}$ can now be computed from the change in the volume below $\mathbb{T}$ and the divergence of the horizontal flow below $\mathbb{T}$ (appendix B). By integrating the volume conservation equation ($\partial_t h_{\text{iso}} + \partial_x U + \omega_{\text{dia}} = 0$, appendix B) over an analysis period of 5 days, the time-averaged diapycnal velocity is given by

$$\overline{\omega_{\text{dia}}}^t(x, \mathbb{T}) = -\frac{h_{\text{iso}}(x, \mathbb{T}, t_0 + \Delta t) - h_{\text{iso}}(x, \mathbb{T}, t_0)}{\Delta t} - \partial_x \overline{U}^t, \tag{8}$$

where $\Delta t = 5$ days, t_0 is the beginning of the analysis period, and $\overline{\cdot}^t$ denotes the 5-day time averages.

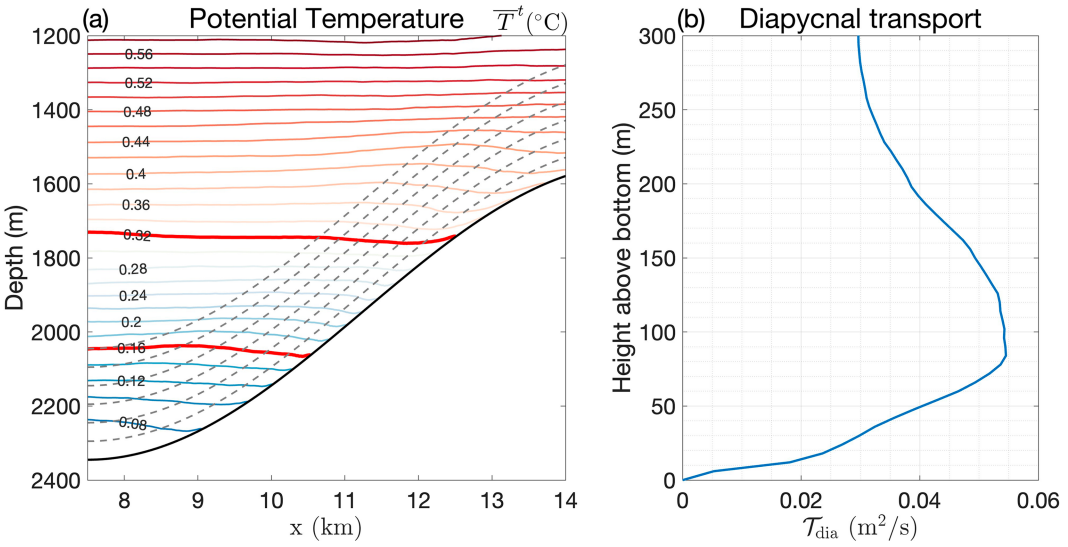

FIG. 7. The diapycnal transport calculated using the integrated isopycnal fluxes. (a) 5-day averaged potential temperature. The control volume is chosen with two bounding isopycnals [0.16° and 0.32°C, the thick red curves in (a)], the sloping bottom, and a moving upper boundary as a function of HAB (gray dashed curves with an interval of 50 m). (b) Diapycnal transport within the control volume as a function of HAB.

To quantify the time-averaged diapycnal transport over the slope, we define a control volume bounded by the bottom topography, two temperature surfaces or equivalently isopycnals (thick red curves in Fig. 7a) covering the steepest part of the slope. The fourth boundary of the control volume is varied to quantify the diapycnal transport as a function of height above the bottom (gray dashed lines in Fig. 7a). The diapycnal transport ($\mathcal{T}_{\rm dia}$, Fig. 7b) is computed by integrating the time-averaged diapycnal velocity $\overline{\omega_{\rm dia}}^t$ within the control volume (details in appendix B).

The diagnosed transport confirms that there is diapycnal upwelling within the lower 80 m above the seafloor (where $\mathcal{T}_{\rm dia}$ increases with height above the bottom) and diapycnal downwelling above (where $\mathcal{T}_{\rm dia}$ decreases with height above the bottom). While this spatial pattern aligns with prior studies examining water mass transformation adjacent to sloping topography using prescribed mixing profiles (e.g., Ferrari et al. 2016; McDougall and Ferrari 2017), the upwelling layer appears considerably thicker in our simulations. We suspect that the thick upwelling layer is not solely attributable to the bottom trapped mixing that develops during the flood phase which results in a strong convergence of turbulent buoyancy fluxes near the seafloor (as seen in earlier studies employing prescribed mixing). It could also involve a contribution from the convective events that develop during the ebb phase. These events result in a convergence of turbulent buoyancy fluxes, which, despite being small in magnitude, can lead to nonnegligible water mass transformation, particularly when coupled with the weak stratification. Furthermore, the thickening of the upwelling layer may result from the 5-day averaging operation. This averaging spreads the intense upwelling observed during the flood phase over the broader turbulent boundary layer span, when combined with the elevated isopycnal positions occurring during the ebb phase.

4. Passive tracer evolution

Further insights into the diagnostics of diapycnal transport can be gained by observing the evolution of passive tracers. To that purpose, we release numerical passive tracers at different locations along the slope.

Two patches of passive tracers are released with an initial profile given by a 2D Gaussian function:

$$c_0(x, z) = e^{-[(x-x_0)^2/(2\sigma_x^2)+(z-z_0)^2/(2\sigma_z^2)]}, \tag{9}$$

with $\sigma_x = 500$ m and $\sigma_z = 40$ m. One is released in the deepest trough of the topography ($x_0 = 7.5$ km and $z_0 = -2330$ m) 15 m above the bottom. The other is released at the midslope location ($x_0 = 11.25$ km and $z_0 = -1900$ m) 40 m above the bottom (Figs. 8a,b). The tracers are evolved for 15 tidal cycles after the initial spinup period of 25 days. They are advected back and forth by fast-reversing tidal flows and mixed by turbulent mixing across isopycnals, resulting in a broadening distribution across the slope via shear dispersion (Figs. 8c,d).

The diapycnal flow experienced by the tracer patch can be estimated through the temporal evolution of the center of mass of the tracer patch computed as the tracer-weighted buoyancy, $\overline{b}$, where the overbar denotes the tracer-weighted average:

$$\overline{(\cdot)} \equiv \frac{\iiint (\cdot) c \, dx \, dy \, dz}{\iiint c \, dx \, dy \, dz}, \tag{10}$$

where c is the tracer concentration. Ruan and Ferrari (2021) show that the evolution of $\overline{b}$ is determined by the divergence of the tracer-weighted diffusive buoyancy flux:

$$\partial_t \overline{b} = 2\overline{\nabla \cdot (\kappa \nabla b)}. \tag{11}$$

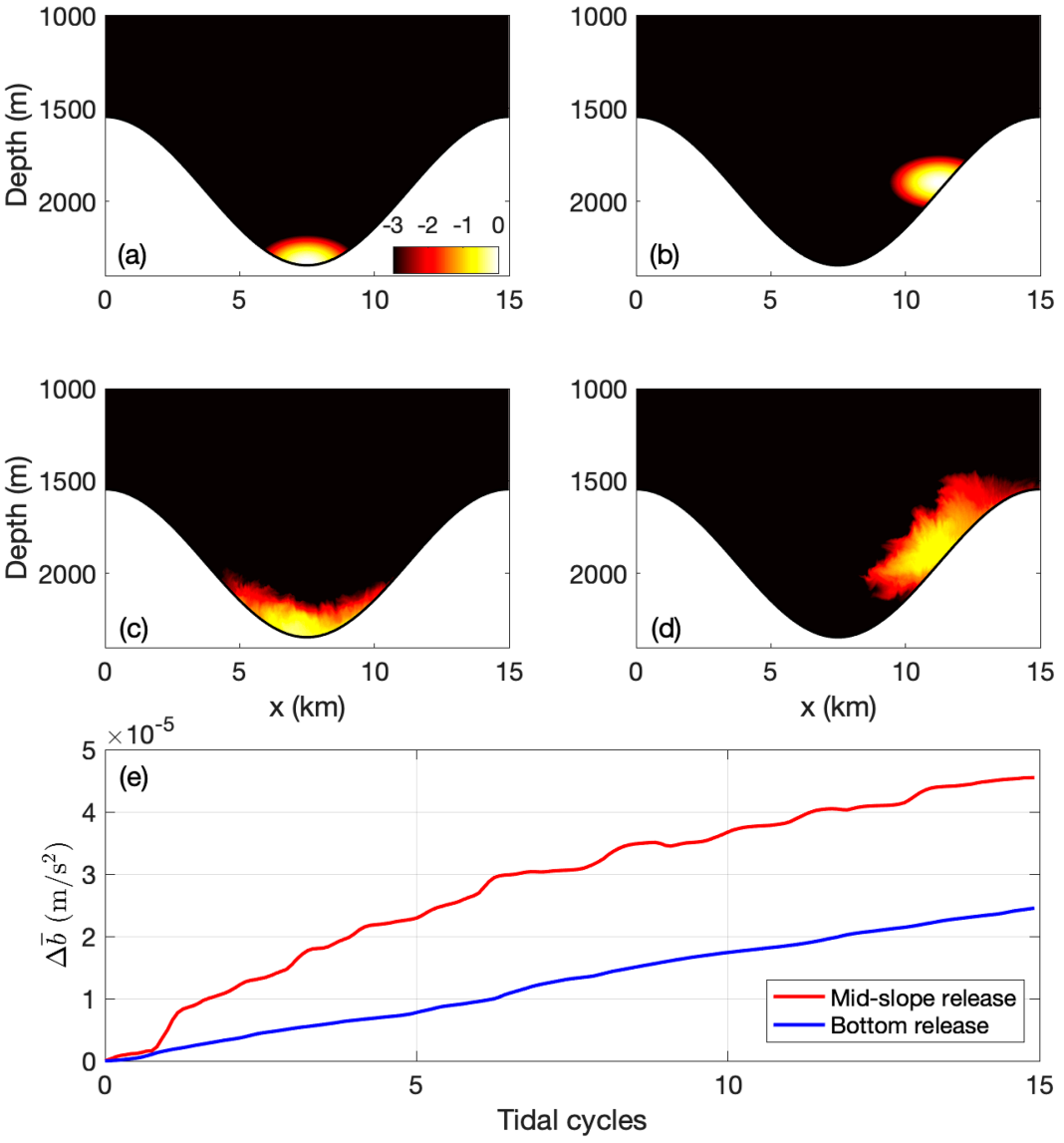

FIG. 8. The concentration of two tracer patches (a),(b) just after release at the bottom and midslope, respectively, and (c),(d) after 15 tidal cycles. Color shading is logarithmic in tracer concentration. (e) The increase in buoyancy of the center of mass of the two tracer patches as a function of time.

The equation confirms that a tracer released in a region of convergent flux will tend to drift toward lighter isopycnals.

In our simulation, the center of mass of the tracer increases for both tracer patches over the 15 tidal cycles implying that the tracers experience net upwelling across density surfaces under the influence of tidal mixing (Fig. 8e). The tracer patch released further up the slope does upwell more rapidly, but the difference in diapycnal upwelling rates between the two patches is not as significant as one might anticipate. This is despite the fact that the tracer released near the critical topographic slope is subjected to greater shears and more intense mixing. However, the tracer released at the lower position is unique because it can only move upward toward areas of lighter buoyancy. Consequently, it is inevitably subjected to more diapycnal upwelling than any tracer released higher on the slope, even if it undergoes the same level of mixing. Figure 8e further shows that the patch released at midslope decreases with time as the tracer spreads away from the strong mixing along the boundary (see also Fig. 9).

The evolution of the center of mass of the tracer patch released near the critical topography, $\partial_t \overline{b}$, is plotted on top of the evolution of the local horizontal velocity and stratification (Fig. 9). The rapid increase in the center of mass of the tracer coincides with positive velocity, clearly indicating that the tracer moves toward lighter buoyancy during the flood phase of the tidal cycle, when the horizontal flow is up the slope and the stratification is largest. Instead, the center of mass hardly changes during the ebb phase. This is consistent with our

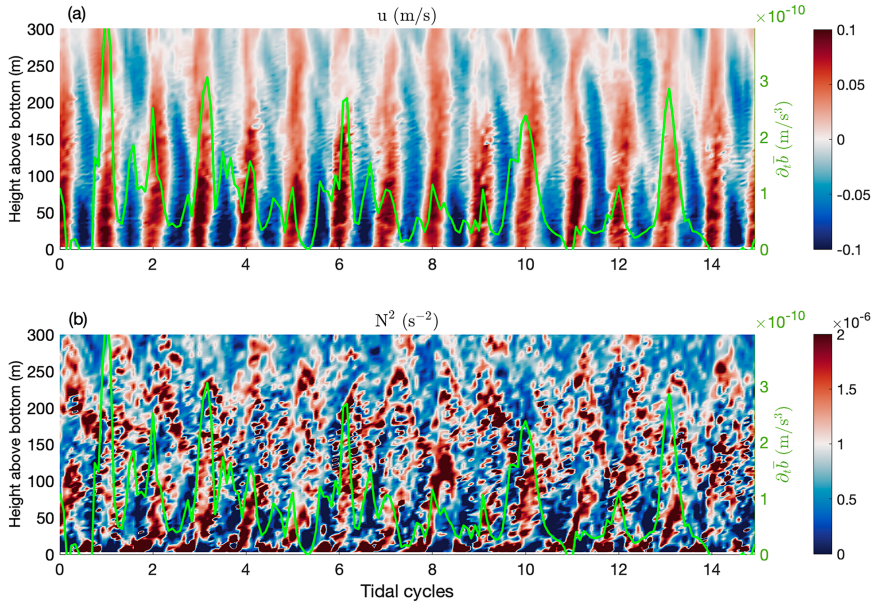

FIG. 9. Time series of (a) zonal velocity u and (b) stratification N^2 at the midslope location during the 15 tidal cycles where passive tracers are evolved. The green curve represents the rate of change of the tracer-weighted buoyancy $\partial_t \overline{b}$ for the tracer released at the same midslope position.

previous analysis, which identified the flood phase as the time when shear-driven mixing drives a strong cross-slope diapycnal flow. The weaker diapycnal flow during the ebb phase, despite vigorous convection, instead echoes the comment by Garrett (1979) that mixing already mixed waters in bottom boundary layers contributes little to local water mass transformation. Finally, we quantified a tracer-based diapycnal diffusivity according to Ruan and Ferrari (2021) and found that this diffusivity peaks in the flood phase, reaching $O(10^{-2})$ m^2 s^{-1}, while being significantly weaker in the ebb phase (figure not shown). This indicates that the growth rate of the tracer variance in buoyancy space is punctuated by rapid bursts during the flood phase of the tidal cycles, rather than approaching a constant (resulting in a linear growth of variance). This calls into question the common approach of estimating diffusivities from tracer release experiments from the tracer spreading at two times weeks to months apart.

5. Conclusions and discussion

We used a nonhydrostatic, two-dimensional numerical model to study turbulent mixing and the associated water mass transformation generated by a barotropic tidal flow interacting with steeply sloping topography. The topographic slope was chosen to be close to critical such that the reflection of tidal beams generated strong shears along the topography. Shear-driven instabilities and vigorous diapycnal mixing developed over a few tens of meters above the seafloor during the flood phase of the tide, when the flow was directed up the slope and the tidal shear acted to restratify the bottom boundary layer. Weak diapycnal mixing was instead observed during the ebb phase, when the flow was directed down the slope and the shear reduced the stratification of the bottom boundary layer. During this phase, strong convective overturns developed up to a couple hundred meters above the seafloor, but they acted on weakly stratified waters, thus resulting in little diapycnal mixing. The small-scale shear-driven mixing highlighted in our study aligns with previous observations, such as those by Farmer and Armi (1999) and Cyr and Van Haren (2016), and should be incorporated into future parameterizations of internal tide–related turbulent mixing, which often focus excessively on large-scale overturns associated with convective mixing (e.g., Klymak and Legg 2010; Gayen and Sarkar 2011; Chalamalla and Sarkar 2015).

This scenario is very different from the more classic picture where a tidal flow interacts with gentle topography with small-scale corrugations, leading to the radiation of waves that interact and break away from topography. Rather than a statistically stationary distribution of mixing decaying over a few hundred meters above the seafloor, in the scenario considered in this study, strong mixing is confined to a few tens of meters above the seafloor and occurs in bursts confined to one phase of the tidal cycle. This result underscores the importance of incorporating temporal variability of tidal forcing when calculating buoyancy flux and diapycnal transport. Furthermore, it prompts caution in interpreting mixing measurements near sloping topography across different phases of the tidal cycle, as a constant Γ is often used to convert from energy dissipation rates to turbulent diffusivity (e.g., Moum et al. 2002; Aucan et al. 2006; Nash et al. 2007; Alford et al. 2011; Martini et al. 2013). Finally, the time-averaged diapycnal transport displays a dipole pattern, akin to prior studies, with upwelling near the seafloor and downwelling above it. However, the time-averaged picture hides the fact that the upwelling occurs in short bursts rather than continuously.

There are several differences between the idealized numerical setup and real ocean environment that are worth discussing.

First, the sloping bottom is rather smooth in the model without any realistic bottom roughness such as that associated with sills, hills, and seamounts. We speculate that with real-ocean roughness, the simulated thin (~15 m) and drag-controlled layer close to the seafloor would likely grow much thicker. This could result in a stronger and more extended bottom shear that could lead to mixing over a much thicker layer and possibly even overturning events. If this hypothesis holds true, both convection and shear mixing could take place in the flood phase. Second, this study only considers a barotropic tidal flow interacting with sloping topography. In the real ocean, the bottom flow can also consist of internal tides of different vertical modes leading to different responses near the bottom. Three-dimensional lateral exchange is another process we do not address in this study. Inertial oscillations, asymmetries of topography in the along-slope direction, and submesoscale instabilities could all facilitate mass exchanges between the boundary layer and the interior ocean, complicating the interpretation of the measured turbulent buoyancy fluxes and their effects on the local diapycnal transport.

A field campaign has recently been completed in a submarine canyon in the Rockall Trough where strong tidal motions prevail. The campaign collected an extensive set of measurements of turbulence with microstructure probes and a fluorescent dye release experiment. Consistent with our study, vigorous mixing events develop along the canyon seafloor when the tidal shear is positive and thus destabilizes the water column (Wynne-Cattanach et al. 2024). Unlike in our idealized study, mixing extends 100–200 m above the seafloor and a positive tidal shear develops at different phases of the tide depending on the along-canyon location. These differences likely stem from our idealization of a smooth topography and a simple barotropic tidal forcing.

Despite its idealization, our study offers useful insights into the interpretation of measured mixing rates, turbulent fluxes, and their influences on the diapycnal transport. Past modeling studies have considered the effect of wave-breaking-induced mixing in a heavily averaged form, but did not consider the spatial heterogeneity and temporal intermittency associated with tidally induced mixing near the seafloor. Future efforts in mapping the diapycnal pathways in the abyssal ocean need to take into account both dynamical regimes.

Acknowledgments. We dedicate this paper to a great friend and scientist, Jim Ledwell, who passed away before the completion of this paper. Jim's insight and expertise in turbulent mixing will be greatly missed. We also thank Alberto Naveira Garabato, Matthew Alford, and Gunnar Voet for insightful discussions. Support through NSF Awards OCE-1756324 and OCE-2343008 is gratefully acknowledged. We also acknowledge high-performance computing support from the Derecho system (https://doi.org/10.5065/qx9a-pg09) provided by the NSF National Center for Atmospheric Research (NCAR), sponsored by the National Science Foundation.

Data availability statement. The data used in this study can be obtained at https://doi.org/10.5281/zenodo.10502420.

APPENDIX A

Quantification of Numerical Mixing

We introduce the diagnostics and compare explicitly resolved turbulent mixing with effective mixing, which encompasses both the resolved component and numerical mixing. This analysis demonstrates that numerical mixing has a negligible impact on our study. As introduced earlier, the resolved dissipation rate of temperature variance is quantified as $\chi_T = \kappa_i |\partial x_i T|^2$, where the temperature gradient is explicitly computed using pointwise model output. The effective dissipation rate, on the other hand, is calculated based on the temperature variance equation:

$$\chi_T^{\text{eff}} = -\frac{1}{V}\left[\frac{d}{dt}\int \frac{T^2}{2} dV - \int \nabla \cdot (\kappa T \nabla T) dV\right], \tag{A1}$$

$$= -\frac{1}{V}\left(\frac{d}{dt}\int \frac{T^2}{2}\, dV - \int \kappa T \nabla T\, dS\right), \tag{A2}$$

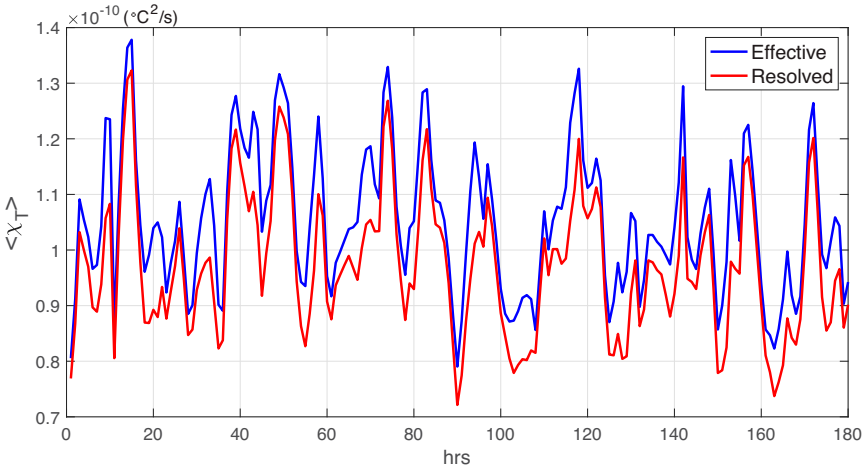

FIG. A1. Effective and resolved volume-averaged dissipation rate of temperature variance.

where S is the surface area of the control volume at which the product of diffusive temperature flux and temperature itself is evaluated. The diagnosed dissipation rates in Fig. A1 demonstrate the negligible impact of numerical mixing in our high-resolution simulations.

APPENDIX B

Quantification of Diapycnal Transport

In this appendix, we derive the equation used in section 3b to diagnose the diapycnal transport.

First, we integrate the volume conservation equation over the area depicted in Fig. B1, vertically from the ocean bottom $z = \eta_b(x)$ to an isopycnal $z = \eta(x, t)$ and horizontally between $x = x_1$ and $x = x_2$ (Fig. B1),

$$\iint_{\delta A} \nabla \cdot \mathbf{u}\, dx\, dz = 0. \tag{B1}$$

We indicate the integration area by $\delta A = h_{\text{iso}}\Delta x$, where h_{iso} is the height of the instantaneous isopycnal above the bottom [Eq. (7)], and $\Delta x = x_2 - x_1$.

Applying the divergence theorem to this integral, we have

$$\int_{\eta_b}^{\eta} \mathbf{u}\cdot\hat{\mathbf{x}}\, dz\big|_{\text{right}} - \int_{\eta_b}^{\eta} \mathbf{u}\cdot\hat{\mathbf{x}}\, dz\big|_{\text{left}} + \int_{x_1}^{x_2} \mathbf{u}\cdot\hat{\mathbf{n}}\, dx\big|_{\text{top}} - \int_{x_1}^{x_2} \mathbf{u}\cdot\hat{\mathbf{n}}\, dx\big|_{\text{bottom}} = 0, \tag{B2}$$

where $\hat{\mathbf{x}}$ is the unit vector normal to the two lateral boundaries of the region δA and $\hat{\mathbf{n}}$ is the unit vector normal to the top and bottom boundaries. The last term in Eq. (B2) is zero because of the no-flux boundary condition at the ocean bottom.

Next we decompose the Eulerian velocity $\mathbf{u}$ into two components: the velocity of the isopycnal ($\mathbf{u}_s = \partial_t h_{\text{iso}}$) and the diapycnal velocity ($\mathbf{u}_d = \mathbf{u} - \mathbf{u}_s$), i.e., the component of the velocity that crosses the isopycnal. With these definitions, Eq. (B2) becomes

$$\Delta\int_{\eta_b}^{\eta} \mathbf{u}\cdot\hat{\mathbf{x}}\, dz + \int_{x_1}^{x_2} (\mathbf{u} - \mathbf{u}_s)\cdot\hat{\mathbf{n}}\, dx\big|_{\text{top}} + \int_{x_1}^{x_2} \mathbf{u}_s\cdot\hat{\mathbf{n}}\, dx\big|_{\text{top}} = 0, \tag{B3}$$

where the symbol Δ denotes the lateral difference. Dividing Eq. (B3) by $\Delta x = x_2 - x_1$ and taking the limit $\Delta x \to 0$, we have

$$\frac{\partial}{\partial x}\int_{\eta_b}^{\eta} \mathbf{u}\cdot\hat{\mathbf{x}}\, dz + \mathbf{u}_d\cdot\hat{\mathbf{n}}\big|_{\text{top}} + \frac{\partial h_{\text{iso}}}{\partial t} = 0. \tag{B4}$$

Therefore, the diapycnal velocity $\omega_{\text{dia}} = \mathbf{u}_d\cdot\hat{\mathbf{n}}\big|_{\text{top}}$ across the isopycnal η can be computed as

$$\omega_{\text{dia}} = -\partial_x U - \partial_t h_{\text{iso}}, \tag{B5}$$

where U is the horizontal transport below the isopycnal η [equivalently, the potential temperature $\mathbb{T}$, Eq. (6)].

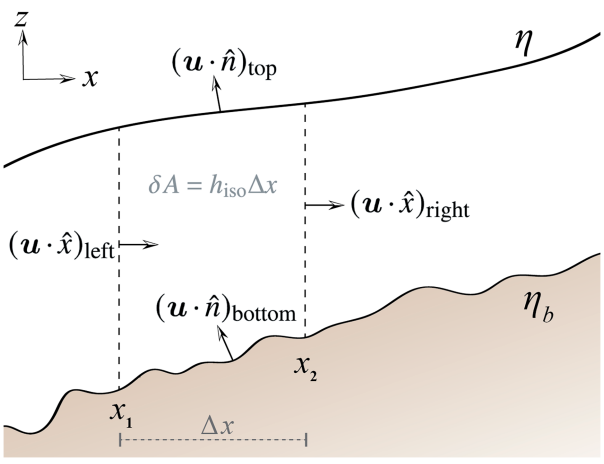

FIG. B1. Schematic illustrating the area used for integrating the volume conservation equation.

The diapycnal transport across the isopycnal/isotherm $\mathbb{T}$ is now given by the integral in x for fixed $\mathbb{T}$ of $\omega_{\text{dia}}(x, \mathbb{T})$. As illustrated in Fig. B1, we are after the diapycnal transport between the seafloor and a height above the bottom $\boldsymbol{h}$ (defined in section 3b). We therefore carry the x integral between the two x coordinates where the isopycnal intersects the seafloor and $z = \boldsymbol{h}$, respectively.

To obtain the averaged diapycnal transport over many tidal cycles, we take the 5-day average of the diapycnal velocity $\overline{\omega_{\text{dia}}}^{t}(x, \mathbb{T})$ and the x integral is taken between the positions where the 5-day averaged isopycnal intersects the seafloor, x_0, and the $z = \boldsymbol{h}$ along the same isopycnal, $x_{\boldsymbol{h}}$:

$$\mathcal{T}_{\text{dia}}(\mathbb{T}, \boldsymbol{h}) = \int_{x_0}^{x_{\boldsymbol{h}}} \overline{\omega_{\text{dia}}}^{t}\, dx. \tag{B6}$$

Last, to reduce noise due to the turbulent nature of the flow, we average the results over a range of isopycnals.

While the final estimate is somewhat uncertain due to the substantial variation in stratification across different tidal phases, especially when potential temperature/density does not vary monotonically with depth, we verified that the results are not sensitive to the specific potential temperature intervals used to bound the averaging volume.

REFERENCES

Alford, M. H., and Coauthors, 2011: Energy flux and dissipation in Luzon strait: Two tales of two ridges. *J. Phys. Oceanogr.*, **41**, 2211–2222, https://doi.org/10.1175/JPO-D-11-073.1.

Aucan, J., M. A. Merrifield, D. S. Luther, and P. Flament, 2006: Tidal mixing events on the deep flanks of Kaena ridge, Hawaii. *J. Phys. Oceanogr.*, **36**, 1202–1219, https://doi.org/10.1175/JPO2888.1.

Buijsman, M. C., S. Legg, and J. Klymak, 2012: Double-ridge internal tide interference and its effect on dissipation in Luzon strait. *J. Phys. Oceanogr.*, **42**, 1337–1356, https://doi.org/10.1175/JPO-D-11-0210.1.

Callies, J., and R. Ferrari, 2018: Dynamics of an abyssal circulation driven by bottom-intensified mixing on slopes. *J. Phys. Oceanogr.*, **48**, 1257–1282, https://doi.org/10.1175/JPO-D-17-0125.1.

Chalamalla, V. K., and S. Sarkar, 2015: Mixing, dissipation rate, and their overturn-based estimates in a near-bottom turbulent flow driven by internal tides. *J. Phys. Oceanogr.*, **45**, 1969–1987, https://doi.org/10.1175/JPO-D-14-0057.1.

Cyr, F., and H. Van Haren, 2016: Observations of small-scale secondary instabilities during the shoaling of internal bores on a deep-ocean slope. *J. Phys. Oceanogr.*, **46**, 219–231, https://doi.org/10.1175/JPO-D-15-0059.1.

Dauhajre, D. P., M. J. Molemaker, J. C. McWilliams, and D. Hypolite, 2021: Effects of stratification on shoaling internal tidal bores. *J. Phys. Oceanogr.*, **51**, 3183–3202, https://doi.org/10.1175/JPO-D-21-0107.1.

Dauxois, T., and W. R. Young, 1999: Near-critical reflection of internal waves. *J. Fluid Mech.*, **390**, 271–295, https://doi.org/10.1017/S0022112099005108.

de Lavergne, C., G. Madec, J. Le Sommer, A. J. G. Nurser, and A. C. Naveira Garabato, 2016: On the consumption of Antarctic Bottom Water in the abyssal ocean. *J. Phys. Oceanogr.*, **46**, 635–661, https://doi.org/10.1175/JPO-D-14-0201.1.

Eriksen, C. C., 1982: Observations of internal wave reflection off sloping bottoms. *J. Geophys. Res.*, **87**, 525–538, https://doi.org/10.1029/JC087iC01p00525.

Farmer, D., and L. Armi, 1999: Stratified flow over topography: The role of small-scale entrainment and mixing in flow establishment. *Proc. Roy. Soc. London*, **455A**, 3221–3258, https://doi.org/10.1098/rspa.1999.0448.

Ferrari, R., 2014: What goes down must come up. *Nature*, **513**, 179–180, https://doi.org/10.1038/513179a.

——, A. Mashayek, T. J. McDougall, M. Nikurashin, and J.-M. Campin, 2016: Turning ocean mixing upside down. *J. Phys. Oceanogr.*, **46**, 2239–2261, https://doi.org/10.1175/JPO-D-15-0244.1.

Garrett, C., 1979: Comment on 'some evidence for boundary mixing in the deep ocean' by Laurence Armi. *J. Geophys. Res.*, **84**, 5095, https://doi.org/10.1029/JC084iC08p05095.

——, P. MacCready, and P. Rhines, 1993: Boundary mixing and arrested Ekman layers: Rotating stratified flow near a sloping boundary. *Annu. Rev. Fluid Mech.*, **25**, 291–323, https://doi.org/10.1146/annurev.fl.25.010193.001451.

Gayen, B., and S. Sarkar, 2011: Boundary mixing by density overturns in an internal tidal beam. *Geophys. Res. Lett.*, **38**, L14608, https://doi.org/10.1029/2011GL048135.

Gregg, M. C., E. A. D'Asaro, J. J. Riley, and E. Kunze, 2018: Mixing efficiency in the ocean. *Annu. Rev. Mar. Sci.*, **10**, 443–473, https://doi.org/10.1146/annurev-marine-121916-063643.

Howard, L. N., 1961: Note on a paper of John W. Miles. *J. Fluid Mech.*, **10**, 509–512, https://doi.org/10.1017/S0022112061000317.

Jalali, M., A. VanDine, V. K. Chalamalla, and S. Sarkar, 2017: Oscillatory stratified flow over supercritical topography: Wave energetics and turbulence. *Comput. Fluids*, **158**, 39–48, https://doi.org/10.1016/j.compfluid.2016.12.019.

Klymak, J. M., and S. M. Legg, 2010: A simple mixing scheme for models that resolve breaking internal waves. *Ocean Modell.*, **33**, 224–234, https://doi.org/10.1016/j.ocemod.2010.02.005.

——, and Coauthors, 2006: An estimate of tidal energy lost to turbulence at the Hawaiian ridge. *J. Phys. Oceanogr.*, **36**, 1148–1164, https://doi.org/10.1175/JPO2885.1.

——, S. Legg, and R. Pinkel, 2010: A simple parameterization of turbulent tidal mixing near supercritical topography. *J. Phys. Oceanogr.*, **40**, 2059–2074, https://doi.org/10.1175/2010JPO4396.1.

Ledwell, J. R., E. T. Montgomery, K. L. Polzin, L. C. St. Laurent, R. W. Schmitt, and J. M. Toole, 2000: Evidence for enhanced mixing over rough topography in the abyssal ocean. *Nature*, **403**, 179–182, https://doi.org/10.1038/35003164.

Legg, S., and A. Adcroft, 2003: Internal wave breaking at concave and convex continental slopes. *J. Phys. Oceanogr.*, **33**, 2224–2246, https://doi.org/10.1175/1520-0485(2003)033<2224:IWBACA>2.0.CO;2.

——, and K. M. H. Huijts, 2006: Preliminary simulations of internal waves and mixing generated by finite amplitude tidal flow over isolated topography. *Deep-Sea Res. II*, **53**, 140–156, https://doi.org/10.1016/j.dsr2.2005.09.014.

——, and J. Klymak, 2008: Internal hydraulic jumps and overturning generated by tidal flow over a tall steep ridge. *J. Phys. Oceanogr.*, **38**, 1949–1964, https://doi.org/10.1175/2008JPO3777.1.

Lumpkin, R., and K. Speer, 2007: Global ocean meridional overturning. *J. Phys. Oceanogr.*, **37**, 2550–2562, https://doi.org/10.1175/JPO3130.1.

Marshall, J., A. Adcroft, C. Hill, L. Perelman, and C. Heisey, 1997: A finite-volume, incompressible Navier Stokes model for studies of the ocean on parallel computers. *J. Geophys. Res.*, **102**, 5753–5766, https://doi.org/10.1029/96JC02775.

Martini, K. I., M. H. Alford, E. Kunze, S. M. Kelly, and J. D. Nash, 2013: Internal bores and breaking internal tides on the Oregon continental slope. *J. Phys. Oceanogr.*, **43**, 120–139, https://doi.org/10.1175/JPO-D-12-030.1.

Mashayek, A., H. Salehipour, D. Bouffard, C. P. Caulfield, R. Ferrari, M. Nikurashin, W. R. Peltier, and W. D. Smyth, 2017: Efficiency of turbulent mixing in the abyssal ocean circulation. *Geophys. Res. Lett.*, **44**, 6296–6306, https://doi.org/10.1002/2016GL072452.

McDougall, T. J., and R. Ferrari, 2017: Abyssal upwelling and downwelling driven by near-boundary mixing. *J. Phys. Oceanogr.*, **47**, 261–283, https://doi.org/10.1175/JPO-D-16-0082.1.

Miles, J. W., 1961: On the stability of heterogeneous shear flows. *J. Fluid Mech.*, **10**, 496–508, https://doi.org/10.1017/S0022112061000305.

Moum, J. N., D. R. Caldwell, J. D. Nash, and G. D. Gunderson, 2002: Observations of boundary mixing over the continental slope. *J. Phys. Oceanogr.*, **32**, 2113–2130, https://doi.org/10.1175/1520-0485(2002)032<2113:OOBMOT>2.0.CO;2.

Munk, W. H., 1966: Abyssal recipes. *Deep-Sea Res. Oceanogr. Abstr.*, **13**, 707–730, https://doi.org/10.1016/0011-7471(66)90602-4.

Nash, J. D., M. H. Alford, E. Kunze, K. Martini, and S. Kelly, 2007: Hotspots of deep ocean mixing on the Oregon continental slope. *Geophys. Res. Lett.*, **34**, L01605, https://doi.org/10.1029/2006GL028170.

Nikurashin, M., and S. Legg, 2011: A mechanism for local dissipation of internal tides generated at rough topography. *J. Phys. Oceanogr.*, **41**, 378–395, https://doi.org/10.1175/2010JPO4522.1.

Pedlosky, J., 2003: *Waves in the Ocean and Atmosphere: Introduction to Wave Dynamics*. Springer Science and Business Media, 260 pp.

Peltier, W. R., and C. P. Caulfield, 2003: Mixing efficiency in stratified shear flows. *Annu. Rev. Fluid Mech.*, **35**, 135–167, https://doi.org/10.1146/annurev.fluid.35.101101.161144.

Polzin, K. L., 2009: An abyssal recipe. *Ocean Modell.*, **30**, 298–309, https://doi.org/10.1016/j.ocemod.2009.07.006.

——, J. M. Toole, J. R. Ledwell, and R. W. Schmitt, 1997: Spatial variability of turbulent mixing in the abyssal ocean. *Science*, **276**, 93–96, https://doi.org/10.1126/science.276.5309.93.

Ruan, X., and R. Ferrari, 2021: Diagnosing diapycnal mixing from passive tracers. *J. Phys. Oceanogr.*, **51**, 757–767, https://doi.org/10.1175/JPO-D-20-0194.1.

Schmidgall, C. R., Y. Si, A. L. Stewart, A. F. Thompson, and A. M. Hogg, 2023: Dynamical controls on bottom water transport and transformation across the Antarctic Circumpolar Current. *J. Phys. Oceanogr.*, **53**, 1917–1940, https://doi.org/10.1175/JPO-D-22-0113.1.

Slinn, D. N., and J. J. Riley, 1996: Turbulent mixing in the oceanic boundary layer caused by internal wave reflection from sloping terrain. *Dyn. Atmos. Oceans*, **24**, 51–62, https://doi.org/10.1016/0377-0265(95)00425-4.

Smyth, W. D., J. N. Moum, and D. R. Caldwell, 2001: The efficiency of mixing in turbulent patches: Inferences from direct simulations and microstructure observations. *J. Phys. Oceanogr.*, **31**, 1969–1992, https://doi.org/10.1175/1520-0485(2001)031<1969:TEOMIT>2.0.CO;2.

St. Laurent, L. C., J. M. Toole, and R. W. Schmitt, 2001: Buoyancy forcing by turbulence above rough topography in the abyssal Brazil Basin. *J. Phys. Oceanogr.*, **31**, 3476–3495, https://doi.org/10.1175/1520-0485(2001)031<3476:BFBTAR>2.0.CO;2.

Stommel, H., 1957: A survey of ocean current theory. *Deep-Sea Res.*, **4**, 149–184, https://doi.org/10.1016/0146-6313(56)90048-X.

Talley, L. D., 2013: Closure of the global overturning circulation through the Indian, Pacific, and Southern Oceans: Schematics and transports. *Oceanography*, **26** (1), 80–97, https://doi.org/10.5670/oceanog.2013.07.

van Haren, H., 2006: Nonlinear motions at the internal tide source. *Geophys. Res. Lett.*, **33**, L11605, https://doi.org/10.1029/2006GL025851.

——, 2023a: Detailing secondary frontal bore of internal tides breaking above deep-ocean topography. *J. Oceanogr.*, **79**, 581–592, https://doi.org/10.1007/s10872-023-00699-0.

——, 2023b: Internal tidal sloshing and a non-linear wave source away from topography. *Deep-Sea Res. I*, **196**, 104021, https://doi.org/10.1016/j.dsr.2023.104021.

——, F. Mienis, and G. Duineveld, 2022: Contrasting internal tide turbulence in a tributary of the Whittard Canyon. *Cont. Shelf Res.*, **236**, 104679, https://doi.org/10.1016/j.csr.2022.104679.

——, G. Voet, M. H. Alford, B. Fernández-Castro, A. C. Naveira Garabato, B. L. Wynne-Cattanach, H. Mercier, and M.-J. Messias, 2024: Near-slope turbulence in a Rockall canyon. *Deep-Sea Res. I*, **206**, 104277, https://doi.org/10.1016/j.dsr.2024.104277.

Waterhouse, A. F., and Coauthors, 2014: Global patterns of diapycnal mixing from measurements of the turbulent dissipation rate. *J. Phys. Oceanogr.*, **44**, 1854–1872, https://doi.org/10.1175/JPO-D-13-0104.1.

Winters, K. B., 2015: Tidally driven mixing and dissipation in the stratified boundary layer above steep submarine topography. *Geophys. Res. Lett.*, **42**, 7123–7130, https://doi.org/10.1002/2015GL064676.

Wynne-Cattanach, B. L., and Coauthors, 2024: Observations of diapycnal upwelling within a sloping submarine canyon. *Nature*, **630**, 884–890, https://doi.org/10.1038/s41586-024-07411-2.